Testing topological protection of edge states in hexagonal quantum spin Hall candidate materials

Fernando Dominguez,[1,*] Benedikt Scharf,[1,*] Gang Li,[2] Jörg Schäfer,[3] Ralph Claessen,[3] Werner Hanke,[4]
Ronny Thomale,[4] and Ewelina M. Hankiewicz[1]

[1]*Institute for Theoretical Physics and Astrophysics, TP4, University of Würzburg, Am Hubland, 97074 Würzburg, Germany*
[2]*School of Physical Science and Technology, ShanghaiTech University, Shanghai 201210, China*
[3]*Physikalisches Institut and Röntgen Center for Complex Material Systems, University of Würzburg,
Am Hubland, 97074 Würzburg, Germany*
[4]*Institute for Theoretical Physics and Astrophysics, TP1, University of Würzburg, Am Hubland, 97074 Würzburg, Germany*

We analyze the detailed structure of topological edge mode protection occurring in hexagonal quantum spin Hall (QSH) materials. We focus on bismuthene, antimonene, and arsenene on a SiC substrate, which, due to their large bulk gap, may offer new opportunities for room-temperature QSH applications. While time-reversal symmetry is responsible for the principal symmetry protected character of QSH states, the hexagonal edge terminations yield further aspects of crystal symmetry which affect the topological protection. We show that armchair QSH edge states remain gapless under an in-plane magnetic field in the direction along the edge, a hallmark of their topological crystalline protection. In contrast, an out-of-plane magnetic field opens a gap of the order of a few meV within realistic ranges of the parameters. We use these intriguing signatures of armchair QSH edge states to predict experimentally testable fingerprints of their additional topological crystalline character and their helicity emerging in tunneling spectroscopy and ballistic magnetotransport.

Introduction. Dissipationless edge currents in quantum spin Hall (QSH) systems offer unique opportunities for novel device applications [1]. However, one of the main limiting factors of QSH materials is their small bulk band gap requiring cryogenic temperatures [2–5]. In this context, a major step towards the realization of room-temperature QSH applications is bismuthene [6], that is, Bi atoms arrayed in a honeycomb lattice, on a SiC(0001) substrate (Fig. 1). Here, the SiC substrate stabilizes the two-dimensional (2D) layer of Bi atoms and shifts the p_z orbitals of Bi away from the low-energy sector. As a consequence of this orbital filtering, the low-energy physics of the system is governed by the Bi p_x and p_y orbitals [7–9], which in turn give rise to a large atomic on-site spin-orbit coupling (SOC). Such a mechanism, also predicted for Sb or As on a SiC substrate [10], does not only allow for significantly larger bulk gaps (~ 0.8 eV) compared to HgTe [3,4,11–14] and InAs/GaSb [5] quantum wells (QWs) or WTe$_2$ [15–17] layers, but also compared to other hexagonal layers predicted to exhibit helical states, such as jacutingaite [18], silicene [19–22], germanene [19,23], stanene [24,25], [(Bi$_4$Rh)$_3$I]$^{2+}$ [26,27], or graphene on WS$_2$ [28,29].

In QSH systems, time-reversal symmetry (TRS) prevents helical edge states from mixing and gives rise to a protected crossing point in the edge spectrum and a quantized longitudinal conductance. If TRS is broken by an in-plane magnetic field, z-spin-polarized QSH states are expected to mix and a significant gap opens in the edge states [2,3,30]. In contrast, a perpendicular magnetic field B_z (see Fig. 1 for the coordinate
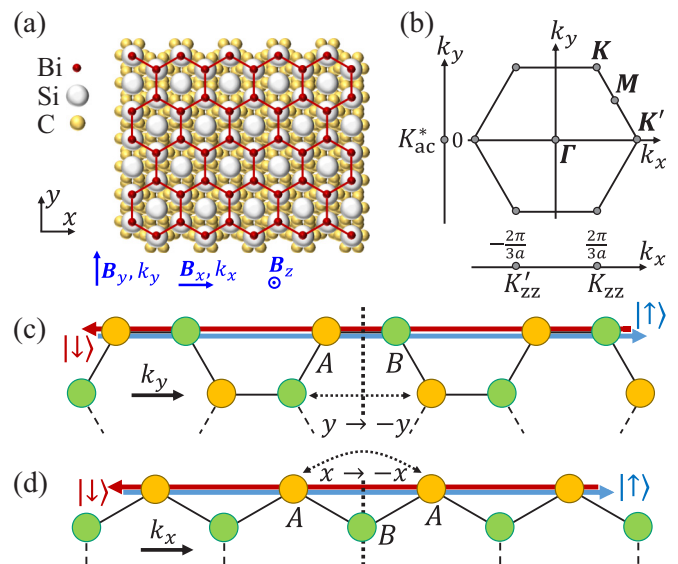

FIG. 1. (a) Schematic representation of a bismuthene layer on a SiC substrate. (b) Brillouin zone and nanoribbon k spaces, denoted as k_x and k_y for ZZ and AC nanoribbons, respectively. The projections of the high-symmetry points to the nanoribbon k spaces are shown in (b). (c) AC and (d) ZZ edges and the effect of the reflection symmetries on the A and B sublattices.

axes) mixes opposite helicities only indirectly via Rashba or Dresselhaus SOC [30,31]. Hence, in the presence of small Rashba and Dresselhaus SOC, nearly gapless helical edge states persist for finite B_z in the ballistic limit. This occurs,

---

*These authors contributed equally to this work.

for example, in QW-based QSH systems, such as symmetric HgTe QWs [32–37].

In this Rapid Communication, we investigate the hierarchy of topological protection in general hexagonal QSH systems with particle-hole symmetry (PHS). We find a generic topological crystalline protection arising from the interplay of PHS and reflection symmetry along the armchair (AC) edge [Figs. 1(c) and 1(d)]. This topological protection manifests itself in gapless AC edge states for any direction of the magnetic field $\boldsymbol{B}$. In contrast, zigzag (ZZ) QSH edge states show a finite gap opening for any direction of $\boldsymbol{B}$ [2,38,39] due to breaking of the reflection symmetry responsible for this protection. Remarkably, even after breaking all symmetries of the system, nanoribbons with AC QSH edge states exhibit a suppressed gap, reminiscent of their topological crystalline protection. We apply these results to bismuthene, antimonene, and arsenene on SiC with well-controlled AC edge termination [40]. This allows us to predict experimentally testable signatures of topological crystalline protection and QSH edge-state helicity in these materials and provides an alternative to nonlocal resistance measurements [13,14] for the confirmation of their topological nature.

Model. We use an 8×8 tight-binding (TB) Hamiltonian describing the low-energy physics of bismuthene, antimonene, and arsenene on SiC [6,10]. For practical purposes, we henceforth use bismuthene parameters [6]. This Hamiltonian is dominated by the Bi p_x and p_y orbitals, localized either on the A or B sites of the honeycomb lattice [Fig. 1(a)] and carrying spin $s = \uparrow / \downarrow$,

$$H = \begin{pmatrix} H_{\uparrow\uparrow} & H_{\uparrow\downarrow} \\ H_{\downarrow\uparrow} & H_{\downarrow\downarrow} \end{pmatrix}, \tag{1}$$

with the basis $|p_{x\uparrow}^A\rangle$, $|p_{y\uparrow}^A\rangle$, $|p_{x\uparrow}^B\rangle$, $|p_{y\uparrow}^B\rangle$, $|p_{x\downarrow}^A\rangle$, $|p_{y\downarrow}^A\rangle$, $|p_{x\downarrow}^B\rangle$, $|p_{y\downarrow}^B\rangle$. Here, the spin-diagonal blocks

$$H_{\uparrow\uparrow/\downarrow\downarrow} = \begin{pmatrix} 0 & \mp i\lambda_{\text{SOC}} & h_{xx}^{AB} & h_{xy}^{AB} \\ \pm i\lambda_{\text{SOC}} & 0 & h_{yx}^{AB} & h_{yy}^{AB} \\ (h_{xx}^{AB})^* & (h_{xy}^{AB})^* & 0 & \mp i\lambda_{\text{SOC}} \\ (h_{yx}^{AB})^* & (h_{yy}^{AB})^* & \pm i\lambda_{\text{SOC}} & 0 \end{pmatrix} \tag{2}$$

contain nearest-neighbor hopping terms (in reciprocal space) $h_{ij}^{AB} = h_{ij}^{AB}(\boldsymbol{k})$ between sublattices A and B parametrized by Slater-Koster integrals [41]. Crucially, Eq. (2) also includes a large effective on-site SOC between the p_x and p_y orbitals, $\lambda_{\text{SOC}} = 435$ meV, responsible for a large bulk band gap at the K/K' points.

In addition, Rashba SOC enters in the off-diagonal terms $H_{\uparrow\downarrow}$, mixing both the spin and sublattice degrees of freedom. This term is proportional to the coupling constant λ_{R} and lifts the degeneracy of the valence bands at K/K', resulting in a valence band splitting of $12\lambda_{\text{R}} \approx 0.4$ eV, also observed experimentally [6]. For the specific form of $H_{\uparrow\downarrow}$, we refer to Refs. [6,41].

Magnetic fields induce orbital effects [Peierls phase in Eq. (1)] and the Zeeman term

$$H_{\text{Z}} = \mu_x B_x + \mu_y B_y + \mu_z B_z. \tag{3}$$
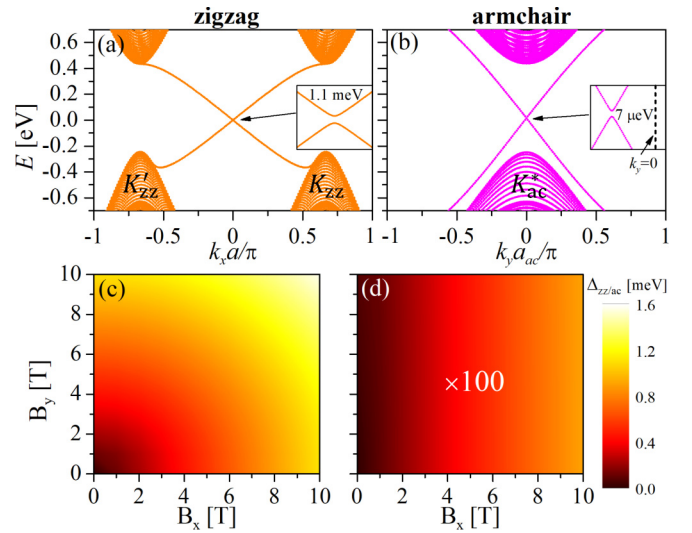

FIG. 2. Dispersions of (a) ZZ and (b) AC nanoribbons with a width of $N_{x/y} = 100$ lattice sites for $B_x = 10$ T. Insets in (a) and (b) show the gaps Δ_{zz} and Δ_{ac} opened between the QSH edge states at finite B_x. (c) and (d) show the dependence of Δ_{zz} and Δ_{ac} on B_x and B_y. Note that Δ_{ac} is multiplied by a factor 100. Here, $a_{\text{ac}} = \sqrt{3}a$ is the length of an AC unit cell and K_{ac}^* is shown in Fig. 1(b).

We compute H_{Z} by applying Löwdin perturbation theory [42,43] around the K point to an *ab initio*-based 52×52 Hamiltonian [44–50] and downfolding this Hamiltonian to the eight bands of our TB Hamiltonian (1). In Eq. (3), the magnetic moments $\mu_{x/y} = g_\parallel \mu_{\text{B}} \mathbf{1} \otimes s_{x/y}/2$ are 8×8 matrices, μ_{B} is the Bohr magneton, $g_\parallel \approx 2$, s_i are spin Pauli matrices, and $\mathbf{1}$ is the 4×4 unit matrix. μ_z is also an 8×8 matrix (see Ref. [41]), which has a nondiagonal spin structure because the higher-energy bands are spin quantized along different axes than the eight bands of our TB model.

Testing the topological protection. We diagonalize the AC and ZZ nanoribbon Hamiltonians obtained from the corresponding discretization of the bulk Hamiltonian given in Eqs. (1)–(3) [41]. We observe (not shown) that in the absence of Rashba SOC, $\lambda_{\text{R}} = 0$, the action of an in-plane magnetic field ($\boldsymbol{B}_\parallel$) always opens a gap in QSH ZZ edge states, while it never does for QSH AC edge states. In turn, for $\lambda_{\text{R}} \neq 0$, a magnetic field along the AC edge does not open a gap, while a finite Δ_{ac}, two orders of magnitude smaller than Δ_{zz} [Figs. 2(a) and 2(b)], opens for the other direction of $\boldsymbol{B}_\parallel$. This strong dependence of Δ_{ac} on the direction of $\boldsymbol{B}_\parallel$ can be seen in Fig. 2(d), very different than for ZZ edges [Fig. 2(c)].

In order to understand these numerical observations, we study the symmetry class and the topological invariant of Eqs. (1)–(3) with $\lambda_{\text{R}} = 0$ and $\boldsymbol{B}_\parallel \neq 0$. The presence of $\boldsymbol{B}_\parallel$ breaks TRS, leaving only PHS. Then, H belongs to symmetry class D. In addition, crystal symmetries, including reflection, rotation, etc., can modify and/or extend the tenfold classification of topological insulators, leading to so-called topological crystalline insulators [51–56], observed by several groups [57–60]. Here, the bulk Hamiltonian exhibits two reflection symmetries $\mathcal{R}(x)$ and $\mathcal{R}(y)$, acting on the Hamiltonian as

$$\mathcal{R}(i)H(\bar{\boldsymbol{k}})\mathcal{R}^{-1}(i) = H(\boldsymbol{k}), \tag{4}$$

where $i = x, y$, $\mathbf{k} = (k_x, k_y)$, and $\bar{\mathbf{k}}$ is equal to $\mathbf{k}$ except for its ith component, which is reflected ($k_i \rightarrow -k_i$). The key difference between $\mathcal{R}(x)$ and $\mathcal{R}(y)$ is that $\mathcal{R}(y) \propto \sigma_x$ mixes A and B sublattices (σ_i are Pauli matrices in sublattice space), while $\mathcal{R}(x) \propto \sigma_0$ is diagonal in this subspace. Following a standard procedure, we find that only the combination of PHS and $\mathcal{R}(y)$ leads to a nontrivial mirror topological invariant, the mirror Chern number MZ_2 [41,53,61,62]. *However, why are ZZ nanoribbons showing an opening of a gap?* At this point, it is important to realize that not all boundary conditions are compatible with $\mathcal{R}(y)$. Indeed, ZZ boundary conditions ($\propto \sigma_z$) do not preserve $\mathcal{R}(y) \propto \sigma_x$ and thus, $\mathbf{B}_{\parallel}$ can open a gap. In turn, $\mathcal{R}(y)$ is compatible with AC boundary conditions and therefore the resulting crossing is topologically protected against $\mathbf{B}_{\parallel}$ [41].

The crystalline topological protection discussed so far can be extended to all hexagonal QSH materials exhibiting PHS, such as the Kane-Mele Hamiltonian. Note, however, that PHS is present only approximately in practice. In the presence of terms breaking PHS, we expect $\mathbf{B}_{\parallel}$ to open a gap. In bismuthene, the main contribution breaking PHS is Rashba SOC. Thus, we now estimate Δ_{ac} opened by $\mathbf{B}_{\parallel}$, when $\lambda_R \neq 0$. To do so, we expand Eq. (1) around $\mathbf{K}/\mathbf{K}'$ [41], yielding $H_{eff} = H_0 + H_R$, with the spin-diagonal contribution

$$H_0 = \hbar v_F (q_x \sigma_x \tau_z + q_y \sigma_y) + \lambda_{SOC} \sigma_z s_z \tau_z, \qquad (5)$$

and the nondiagonal contribution due to Rashba SOC

$$H_R = 3\lambda_R (\sigma_x s_y \tau_z - \sigma_y s_x) + \sqrt{3} q_y a \lambda_R (\sigma_x s_x + \sigma_y s_y \tau_z), \qquad (6)$$

where q_x and q_y are momenta measured from $\mathbf{K}/\mathbf{K}'$, v_F is the Fermi velocity, and σ_i, s_i, and τ_i are Pauli matrices for sublattice, spin, and valley, respectively. Here, the basis is given by $\{|\tau i p_x^B + p_y^B\rangle, |\tau i p_x^A + p_y^A\rangle\}$, with $\tau = \pm 1$ corresponding to the $\mathbf{K}/\mathbf{K}'$ valleys.

Analytical results determined from H_{eff} with AC boundary conditions [63] show no gap opening due to $\mu_y B_y$ because this direction is (trivially) protected by reflection symmetry $\mathcal{R}(y) = \sigma_x s_y$, which takes the role of the helicity operator here. In turn, a Zeeman term in the x direction opens a second-order gap in λ_R, scaling as [41]

$$\Delta_{ac} \approx \frac{3\sqrt{3}a\lambda_R^2}{\lambda_{SOC}\hbar v_F}\mu_B B_x \sim 10^{-2}\mu_B B_x. \qquad (7)$$

Both responses to $\mu_x B_x$ and $\mu_y B_y$ are in good agreement with numerical observations and explain the results shown in Fig. 2(d), where, for example, $B_x = 10$ T ($\mu_B B_x \sim 0.6$ meV) yields $\Delta_{ac} \approx 7$ μeV. Remarkably, even after breaking all symmetries, AC QSH edge states show gaps two orders smaller than those at ZZ edges for in-plane fields.

Following a similar reasoning, $\mu_z B_z$ together with H_R can also open a gap since both contributions break PHS. Here, $\mu_z B_z$ dominates the gap opening due to its nondiagonal structure. Thus, we find comparable AC and ZZ gaps of around a few meV for $B_z = 10$ T ($\Delta_{ac} \sim \Delta_{zz}$, see Fig. 3). Both Δ_{ac} and Δ_{zz} exhibit a B_z-linear dependence with slopes of around 0.2 meV/T. This is the usual behavior expected also for QSH insulators with strong Rashba SOC-like InAs/GaSb QWs [5]. Next, we study signatures of Δ_{ac} and Δ_{zz} and
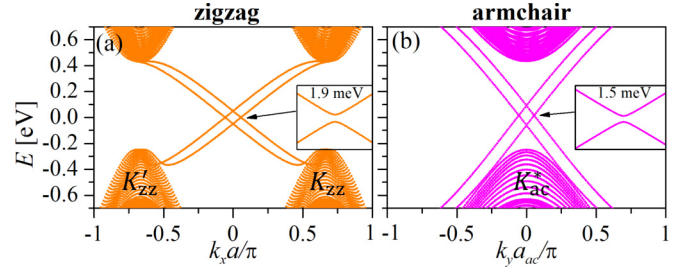
FIG. 3. Dispersions of (a) ZZ and (b) AC nanoribbons with $N_{x/y} = 100$ lattice sites for $B_z = 10$ T. The insets in (a) and (b) show the gaps Δ_{zz} and Δ_{ac} opened between the QSH states at finite B_z.

the topological nature of the QSH states in experimentally accessible quantities.

How to detect the topological nature of the edge states. In Fig. 4, we show the edge local density of states (LDOS) computed from the TB model as a function of energy for ZZ and AC nanoribbons. At $B = 0$, the linear dispersion of the edge states gives rise to a flat LDOS. At finite B, a dip corresponding to Δ_{ac} or Δ_{zz} arises in the edge LDOS, while away from this gap, the edge LDOS is not significantly altered even for $B = 10$ T. Depending on the broadening limited by the parameters of the experimental setup, such as temperature T, Δ_{ac} and Δ_{zz} can be resolved in LDOS measurements. With Δ_{ac} and Δ_{zz} of a few meV, predicted at $B = 10$ T for ZZ (any B) and AC ribbons (B_z), we expect that such gaps could be measured experimentally. This is illustrated in Figs. 4(a) and 4(b), where we have chosen a broadening $\Gamma = 50$ μeV. Note that the opening of the gap in Fig. 4(b) occurs away from $E = 0$ due to Rashba SOC breaking PHS. Remarkably, for AC QSH edge states we predict a tiny nonmeasurable gap of 7 μeV (≈ 80 mK) with B_x and no gap for B_y and consequently a constant signal in the LDOS for both cases. Employing scanning tunneling spectroscopy [6] to monitor the LDOS for different $\mathbf{B}$ orientations, the distinct behavior of AC QSH edge states could serve as a smoking gun to distinguish these states from trivial Rashba edge states, such as those observed in bismuth thin films [64]: For the latter, one would expect a dip in the LDOS as a function of E, independent of the orientation of $\mathbf{B}$, whereas the LDOS of AC QSH edge states exhibits different responses to in-plane $\mathbf{B}$ (flat LDOS) and out-of-plane $\mathbf{B}$ (dip in LDOS).
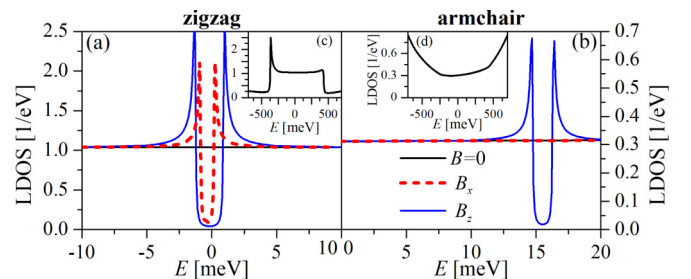
FIG. 4. Edge LDOS of (a) ZZ and (b) AC nanoribbons with $N_{x/y} = 100$ lattice sites close to $E = 0$ for zero and finite $\mathbf{B}$. Insets (c) and (d) show the edge LDOS at $B = 0$ in a wider energy window. We use a Lorentzian broadening $\Gamma = 50$ μeV in (a) and (b) and $\Gamma = 5$ meV in (c) and (d).
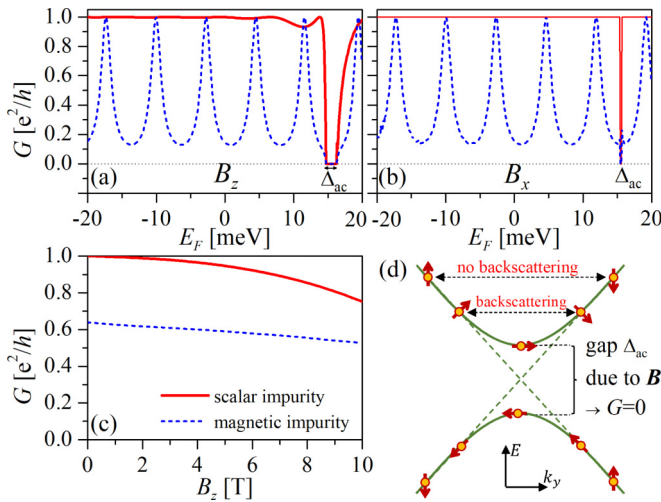
FIG. 5. Conductance G of a single AC edge as a function of the Fermi energy E_F for (a) $B_z = 10$ T and (b) $B_x = 10$ T with two scalar or magnetic impurities present at the edge. (c) Dependence of G on B_z for $E_F = 17$ meV and two impurities. In all panels, the impurities are separated by $d_{imp} = 100$ nm from each other and have a strength of $V_{imp} = 10$ eV Å each in (a) and (b) and $V_{imp} = 5$ eV Å each in (c). (d) Schematic edge-state dispersion with Δ_{ac} opened due to finite $\boldsymbol{B}$ [see (a) and (b)] and schematic spin expectation values $\langle s \rangle$. Note that the actual values and directions of $\langle s \rangle$ depend on the strengths of $\boldsymbol{B}$ and Rashba SOC.

If we focus on a larger energy window, the ZZ edge LDOS also exhibits a clear asymmetry arising from the Rashba-split valence bands. In addition, we can observe signatures of the reduced (1D) dimensionality of the edge states: The van Hove singularities result from bending the linear-dispersion edge state into the continuum as shown in Fig. 4(c) [compare Figs. 2(a) and 3(a)]. Moreover, we observe qualitative differences comparing the LDOS for AC and ZZ edges. While the AC edge LDOS increases for energies outside the bulk band gap [Fig. 4(d)], the ZZ edge LDOS drops significantly at these energies [Fig. 4(c)]. This behavior reflects the fact that AC edge states do not immediately merge with the bulk states at the band edges [compare Figs. 2(b) and 3(b)]. Hence, measurements of the edge LDOS can also elucidate the nature of the boundaries, even at $B = 0$. Indeed, our results for the AC edge LDOS in Fig. 4(d) are qualitatively similar to the LDOS observed experimentally [6].

Another quantity exhibiting signatures of Δ_{ac} or Δ_{zz} and the spin polarization/helicity of the QSH edge states is the magnetoconductance G in the ballistic regime, shown in Fig. 5. Here, we compute G of a single AC edge at finite $\boldsymbol{B}$ via the Fisher-Lee relation [41,65]. In the absence of impurities, the conductance of a single AC edge is perfectly quantized at e^2/h inside the bulk gap for $B = 0$. This quantization remains

for finite $\boldsymbol{B}$, even if scalar impurities are included [66]. The conductance deviates from its quantized value only for the energy window corresponding to the $\boldsymbol{B}$-induced Δ_{ac}, where eventually G drops to zero [Figs. 5(a) and 5(b)]. Here, no propagating states are available as illustrated in Fig. 5(d). If both $\boldsymbol{B}$ and scalar impurities are present, we observe a small reduction with respect to e^2/h close to the gap opening [Fig. 5(a)]. This small deviation reflects the fact that the counterpropagating states are not perfectly spin polarized and can thus scatter even at scalar impurities for a Fermi energy E_F around Δ_{ac} at finite $\boldsymbol{B}$. The suppression of G close to the gap is also shown in Fig. 5(c), which monitors the B_z dependence of G at fixed E_F.

The presence of magnetic impurities significantly reduces G, for both $B = 0$ and finite $\boldsymbol{B}$, independent of the $\boldsymbol{B}$ direction [dashed blue lines in Figs. 5(a)–5(c)]. Here, G decays exponentially with the number of magnetic impurities [41]. Similar to HgTe QWs [33], G exhibits Fabry-Pérot-type oscillations if multiple magnetic impurities are situated at the edge [Figs. 5(a) and 5(b)]. The behavior of G due to impurities, which could be measured in a two-terminal setup, allows us to distinguish between QSH and trivial edge states, since for the latter G would not be quantized, even at $B = 0$.

Outlook. We study the hierarchy of topological protection in general hexagonal QSH systems with PHS. We find a generic topological crystalline protection arising from the interplay of PHS and reflection symmetry along AC edges. This topological protection manifests itself in gapless AC edge states for any direction of $\boldsymbol{B}$. In contrast, ZZ boundary conditions break the reflection symmetry responsible for this protection and give rise to more usual QSH edge states with a finite gap opening for any direction of $\boldsymbol{B}$. Remarkably, even after breaking reflection and PHS, AC QSH states show a suppressed gap, reminiscent of crystalline protection. This special behavior of QSH edge states in $\boldsymbol{B}$ opens the possibility for testing crystalline topological protection and spin helicity in new candidates for QSH systems such as bismuthene, antimonene, and arsenene on SiC. Further, our results have potential applications in spintronics to manipulate/switch spin currents and hybrid superconductor/honeycomb QSH systems, where manipulating the edge-state gap has important consequences for the control of Majorana modes in Josephson junctions [67].

[1] M. Z. Hasan and C. L. Kane, Rev. Mod. Phys. **82**, 3045 (2010); X.-L. Qi and S.-C. Zhang, *ibid.* **83**, 1057 (2011).

[2] C. L. Kane and E. J. Mele, Phys. Rev. Lett. **95**, 146802 (2005); **95**, 226801 (2005).

[3] B. A. Bernevig, T. L. Hughes, and S.-C. Zhang, Science **314**, 1757 (2006).

[4] M. König, S. Wiedmann, C. Brüne, A. Roth, H. Buhmann, L. W. Molenkamp, X.-L. Qi, and S.-C. Zhang, Science **318**, 766 (2007).

[5] I. Knez, R.-R. Du, and G. Sullivan, Phys. Rev. Lett. **107**, 136603 (2011).

[6] F. Reis, G. Li, L. Dudy, M. Bauernfeind, S. Glass, W. Hanke, R. Thomale, J. Schäfer, and R. Claessen, Science **357**, 287 (2017).

[7] C. Wu, Phys. Rev. Lett. **101**, 186807 (2008).

[8] M. Zhang, H.-h. Hung, C. Zhang, and C. Wu, Phys. Rev. A **83**, 023615 (2011).

[9] T. Zhou, J. Zhang, H. Jiang, I. Žutić, and Z. Yang, npj Quantum Mater. **3**, 39 (2018).

[10] G. Li, W. Hanke, E. M. Hankiewicz, F. Reis, J. Schäfer, R. Claessen, C. Wu, and R. Thomale, arXiv:1807.09552 (2018), [Phys. Rev. B (to be published)].

[11] M. König, H. Buhmann, L. W. Molenkamp, T. Hughes, C.-X. Liu, X.-L. Qi, and S.-C. Zhang, J. Phys. Soc. Jpn. **77**, 031007 (2008).

[12] B. Büttner, C. X. Liu, G. Tkachov, E. G. Novik, C. Brüne, H. Buhmann, E. M. Hankiewicz, P. Recher, B. Trauzettel, S. C. Zhang, and L. W. Molenkamp, Nat. Phys. **7**, 418 (2011).

[13] A. Roth, C. Brüne, H. Buhmann, L. W. Molenkamp, J. Maciejko, X.-L. Qi, and S.-C. Zhang, Science **325**, 294 (2009).

[14] C. Brüne, A. Roth, H. Buhmann, E. M. Hankiewicz, L. W. Molenkamp, J. Maciejko, X.-L. Qi, and S.-C. Zhang, Nat. Phys. **8**, 485 (2012).

[15] Z. Fei, T. Palomaki, S. Wu, W. Zhao, X. Cai, B. Sun, P. Nguyen, J. Finney, X. Xu, and D. H. Cobden, Nat. Phys. **13**, 677 (2017).

[16] Z.-Y. Jia, Y.-H. Song, X.-B. Li, K. Ran, P. Lu, H.-J. Zheng, X.-Y. Zhu, Z.-Q. Shi, J. Sun, J. Wen, D. Xing, and S.-C. Li, Phys. Rev. B **96**, 041108 (2017).

[17] S. Wu, V. Fatemi, Q. D. Gibson, K. Watanabe, T. Taniguchi, R. J. Cava, and P. Jarillo-Herrero, Science **359**, 76 (2018).

[18] A. Marrazzo, M. Gibertini, D. Campi, N. Mounet, and N. Marzari, Phys. Rev. Lett. **120**, 117701 (2018).

[19] C.-C. Liu, W. Feng, and Y. Yao, Phys. Rev. Lett. **107**, 076802 (2011).

[20] P. Vogt, P. De Padova, C. Quaresima, J. Avila, E. Frantzeskakis, M. C. Asensio, A. Resta, B. Ealet, and G. Le Lay, Phys. Rev. Lett. **108**, 155501 (2012).

[21] P. Li, X. Li, W. Zhao, H. Chen, M.-X. Chen, Z.-X. Guo, J. Feng, X.-G. Gong, and A. H. MacDonald, Nano Lett. **17**, 6195 (2017).

[22] R. Quhe, R. Fei, Q. Liu, J. Zheng, H. Li, C. Xu, Z. Ni, Y. Wang, D. Yu, Z. Gao, and J. Lu, Sci. Rep. **2**, 853 (2012).

[23] L. Zhang, P. Bampoulis, A. N. Rudenko, Q. Yao, A. van Houselt, B. Poelsema, M. I. Katsnelson, and H. J. W. Zandvliet, Phys. Rev. Lett. **116**, 256804 (2016).

[24] Y. Xu, B. Yan, H.-J. Zhang, J. Wang, G. Xu, P. Tang, W. Duan, and S.-C. Zhang, Phys. Rev. Lett. **111**, 136804 (2013).

[25] W.-X. Ji, C.-W. Zhang, M. Ding, P. Li, F. Li, M.-j. Ren, P.-j. Wang, S.-j. Hu, and S.-s. Yan, Sci. Rep. **5**, 18604 (2015).

[26] B. Rasche, A. Isaeva, M. Ruck, S. Borisenko, V. Zabolotnyy, B. Büchner, K. Koepernik, C. Ortix, M. Richter, and J. van den Brink, Nat. Mater. **12**, 422 (2013).

[27] C. Pauly, B. Rasche, K. Koepernik, M. Liebmann, M. Pratzer, M. Richter, J. Kellner, M. Eschbach, B. Kaufmann, L. Plucinski, C. Schneider, M. Ruck, J. van den Brink, and M. Morgenstern, Nat. Phys. **11**, 338 (2015).

[28] Z. Wang, D.-K. Ki, H. Chen, H. Berger, A. H. MacDonald, and A. F. Morpurgo, Nat. Commun. **6**, 8339 (2015).

[29] M. Gmitra, D. Kochan, P. Högl, and J. Fabian, Phys. Rev. B **93**, 155104 (2016); T. Frank, P. Högl, M. Gmitra, D. Kochan, and J. Fabian, Phys. Rev. Lett. **120**, 156402 (2018).

[30] J. Maciejko, X.-L. Qi, and S.-C. Zhang, Phys. Rev. B **82**, 155310 (2010).

[31] W. Beugeling, N. Goldman, and C. M. Smith, Phys. Rev. B **86**, 075118 (2012).

[32] D. G. Rothe, R. W. Reinthaler, C.-X. Liu, L. W. Molenkamp, S.-C. Zhang, and E. M. Hankiewicz, New J. Phys. **12**, 065012 (2010).

[33] G. Tkachov and E. M. Hankiewicz, Phys. Rev. Lett. **104**, 166803 (2010); Physica E **44**, 900 (2012).

[34] R. Ilan, J. Cayssol, J. H. Bardarson, and J. E. Moore, Phys. Rev. Lett. **109**, 216602 (2012).

[35] J.-C. Chen, J. Wang, and Q.-F. Sun, Phys. Rev. B **85**, 125401 (2012).

[36] B. Scharf, A. Matos-Abiague, and J. Fabian, Phys. Rev. B **86**, 075418 (2012); B. Scharf, A. Matos-Abiague, I. Žutić, and J. Fabian, *ibid.* **91**, 235433 (2015).

[37] M. Kharitonov, S. Juergens, and B. Trauzettel, Phys. Rev. B **94**, 035146 (2016).

[38] J. L. Lado and J. Fernández-Rossier, Phys. Rev. Lett. **113**, 027203 (2014).

[39] S. Rachel and M. Ezawa, Phys. Rev. B **89**, 195303 (2014).

[40] In contrast to many other honeycomb systems, the use of a terraced SiC substrate allows for an efficient control of the edge termination of bismuthene, antimonene, and arsenene on SiC and a well-defined AC edge [68].

[41] See Supplemental Material at http://link.aps.org/supplemental/10.1103/PhysRevB.98.161407 for details on the TB and effective models, symmetries, and the edge-state conductance, which includes Refs. [69–74].

[42] R. Winkler, *Spin-Orbit Coupling Effects in Two-Dimensional Electron and Hole Systems* (Springer, Berlin, 2003).

[43] M. Graf and P. Vogl, Phys. Rev. B **51**, 4940 (1995).

[44] P. Hohenberg and W. Kohn, Phys. Rev. **136**, B864 (1964).

[45] W. Kohn and L. J. Sham, Phys. Rev. **140**, A1133 (1965).

[46] G. Kresse and J. Furthmüller, Phys. Rev. B **54**, 11169 (1996).

[47] P. E. Blöchl, Phys. Rev. B **50**, 17953 (1994).

[48] J. P. Perdew, K. Burke, and M. Ernzerhof, Phys. Rev. Lett. **77**, 3865 (1996).

[49] H. J. Monkhorst and J. D. Pack, Phys. Rev. B **13**, 5188 (1976).

[50] N. Marzari and D. Vanderbilt, Phys. Rev. B **56**, 12847 (1997).

[51] L. Fu, Phys. Rev. Lett. **106**, 106802 (2011).

[52] T. H. Hsieh, H. Lin, J. Liu, W. Duan, A. Bansil, and L. Fu, Nat. Commun. **3**, 982 (2012).

[53] C.-K. Chiu, H. Yao, and S. Ryu, Phys. Rev. B **88**, 075142 (2013).

[54] K. Shiozaki and M. Sato, Phys. Rev. B **90**, 165114 (2014).

[55] Y. Ando and L. Fu, Annu. Rev. Condens. Matter Phys. **6**, 361 (2015).

[56] C.-K. Chiu, J. C. Y. Teo, A. P. Schnyder, and S. Ryu, Rev. Mod. Phys. **88**, 035005 (2016).

[57] S.-Y. Xu, C. Liu, N. Alidoust, M. Neupane, D. Qian, I. Belopolski, J. Denlinger, Y. Wang, H. Lin, L. Wray, G. Landolt, B. Slomski, J. Dil, A. Marcinkova, E. Morosan, Q. Gibson, R. Sankar, F. Chou, R. Cava, A. Bansil, and M. Hasan, Nat. Commun. **3**, 1192 (2012).

[58] Y. Tanaka, Z. Ren, K. Sato, T. Nakayama, T. Souma, S. Takahashi, K. Segawa, and Y. Ando, Nat. Phys. **8**, 800 (2012).

[59] P. Dziawa, B. J. Kowalski, K. Dybko, R. Buczko, A. Szczerbakow, M. Szot, E. Lusakowska, T. Balasubramanian,

B. M. Wojek, M. H. Berntsen, O. Tjernberg, and T. Story, Nat. Mater. **11**, 1023 (2013).

[60] P. Sessi, D. Di Sante, A. Szczerbakow, F. Glott, S. Wilfert, H. Schmidt, T. Bathon, P. Dziawa, M. Greiter, T. Neupert, G. Sangiovanni, T. Story, R. Thomale, and M. Bode, Science **354**, 1269 (2016).

[61] J. C. Y. Teo, L. Fu, and C. L. Kane, Phys. Rev. B **78**, 045426 (2008).

[62] C.-K. Chiu and A. P. Schnyder, Phys. Rev. B **90**, 205136 (2014).

[63] L. Brey and H. A. Fertig, Phys. Rev. B **73**, 235411 (2006).

[64] A. Takayama, T. Sato, S. Souma, T. Oguchi, and T. Takahashi, Phys. Rev. Lett. **114**, 066402 (2015).

[65] D. S. Fisher and P. A. Lee, Phys. Rev. B **23**, 6851 (1981).

[66] G. Tkachov and M. Hentschel, Phys. Rev. B **86**, 205414 (2012).

[67] D. Kuzmanovski, J. Linder, and A. Black-Schaffer, Phys. Rev. B **94**, 180505 (2016).

[68] A. Bandoh, K. Suzuki, Y. Miyasaka, H. Osawa, and T. Sato, Mater. Sci. Forum **778**, 611 (2014).

[69] A. R. Akhmerov and C. W. J. Beenakker, Phys. Rev. B **77**, 085423 (2008).

[70] L. Fu and C. L. Kane, Phys. Rev. B **76**, 045302 (2007).

[71] A. Y. Kitaev, Phys. Usp. **44**, 131 (2001).

[72] M. Kharitonov, J.-B. Mayer, and E. M. Hankiewicz, Phys. Rev. Lett. **119**, 266402 (2017).

[73] E. Prada, P. San-Jose, L. Brey, and H. Fertig, Solid State Commun. **151**, 1075 (2011).

[74] C. Timm, Phys. Rev. B **86**, 155456 (2012).